Type-III Wind Turbine with GFM Features at the Rotor Terminals

Md Sabbir Haider Khan
School of Energy Science and Engg.
IIT Guwahati
Assam, India
sabbir@iitg.ac.in

Hasan Bin Tarique
School of Energy Science and Engg.
IIT Guwahati
Assam, India
s.bintarique@iitg.ac.in

E S N Raju P
School of Energy Science and Engg.
IIT Guwahati
Assam, India
pesnraju88@iitg.ac.in

***Abstract*—Conventional doubly fed induction generators (DFIGs) typically operate in grid-following (GFL) mode, relying on a stiff grid for voltage and frequency support, but increasing renewable penetration and reduced inertia challenge GFL stability. This paper proposes a novel grid-forming (GFM) functionality for a DFIG in which the rotor terminals, connected to the PCC, possess GFM features. The stator windings are interfaced with a machine-side converter (MSC) linked to a dc-link capacitor and an integrated battery energy storage system (BESS), which regulates the dc-link voltage and provides bidirectional energy exchange during super-synchronous and sub-synchronous modes. To develop the GFM control, the DFIG is modeled in the rotor reference frame, and a hierarchical control architecture is introduced, consisting of a droop stage, a magnetizing current control stage, and an inner current control stage. The proposed scheme enables the DFIG to autonomously establish voltage and frequency at the rotor terminals while maintaining stable dc-link operation and effective power balance. MATLAB/Simulink simulations validate the strategy under various operating conditions, demonstrating GFM features at the rotor terminals.**

***Index Terms*—Type-III Wind Turbines, Grid-Forming (GFM) Control, Droop Control, Standalone DFIG, Battery Energy Storage System (BESS).**

I. Introduction

During the past several decades, the depletion of traditional energy resources and their negative environmental effects have driven global efforts toward renewable energy technologies. Among these options, wind energy has experienced rapid growth, exceeding 1.1 TW of global installed capacity by 2024 across 124 countries, with 117 GW added in 2024 alone [1].

Wind power systems (WPS) employ various generator types, most commonly permanent magnet synchronous generators (PMSG) and doubly fed induction generators (DFIG). The DFIG is widely preferred due to its high controllability and relatively low cost. In typical DFIG setups, the stator is directly linked to the grid, while the rotor is interfaced through a back-to-back converter via slip rings.

Most DFIG-based WPS operates in grid-following (GFL) mode, where the converter behaves as a current source and the grid is assumed to be stiff. Increasing wind penetration reduces grid inertia and short-circuit strength, raising risks of voltage and frequency instability.

To address these challenges, the grid-forming (GFM) architecture has been introduced. Unlike GFL operation, GFM operation allows a DFIG to behave as an independent voltage source, establishing its own frequency and enabling seamless islanded operation and inherent frequency support [2]–[4]. When GFM control is applied, key considerations include the energy reserving scheme, dc-link voltage control strategy, and coordinated control of the machine-side converter (MSC) and grid-side converter (GSC). For DFIGs, GFM functions are typically achieved by controlling the MSC to establish stator voltage and frequency, while the GSC regulates the dc-link voltage. If a battery energy storage system (BESS) is connected to the dc-link, it can instead regulate the dc-link voltage [5].

Since frequency support requires energy reserves, deloaded operation becomes necessary, and MPPT is no longer maintained. However, when a BESS is integrated and GFM control is implemented through the GSC, MPPT becomes possible.

GFM functions in DFIGs are mainly implemented using droop control and virtual synchronous generator (VSG) control. In droop-controlled DFIGs, the active power–frequency ($P-\omega$) and reactive power–voltage ($Q-V$) loops determine stator voltage magnitude and frequency references. Several studies employ indirect stator flux orientation (ISFO)-based droop control, where the magnetizing current regulates stator flux while the excitation current loop provides the d-axis rotor current reference.

A recently reported grid-tied DFIG configuration operates the rotor at grid frequency while the stator runs at slip frequency, feeding slip power through the MSC and GSC. This reduces rotor core utilization, machine size, weight, and core losses, yielding a higher torque-to-weight ratio and improved efficiency [10], [11].

Inspired by this concept, the present work proposes implementing GFM functions at the rotor terminals instead of the stator terminals. The DFIG develops its own voltage and frequency through MSC control at the stator side, with no GSC; instead, a BESS regulates the dc-link voltage. To the authors' knowledge, this alternative rotor-side GFM configuration has not been previously explored. The proposed control is mathematically modeled and validated using MATLAB/Simulink simulations.

Section II presents the test system and dynamic modeling, Section III introduces the GFM control strategy, Section IV

979-8-3315-8138-1

provides simulation results, and Section V concludes with key findings and potential extensions.

II. System Description and Dynamic Modeling

A. DFIG System Under Consideration

Fig. 2 illustrates the proposed DFIG system integrated with a BESS. The rotor windings are directly connected to the point of common coupling (PCC), which interfaces with the grid in both grid-connected and islanded modes. The stator windings are connected to a machine-side converter (MSC) coupled with a DC-link capacitor C_{dc} and interfaced with the BESS. The rotor terminals operate with *grid-forming* (GFM) functionality at the PCC, while the stator side connects to the BESS through the MSC. The MSC establishes GFM behavior, and the battery controller maintains constant DC bus voltage by balancing power exchange between the DFIG and the BESS.

During *sub-synchronous* operation, slip is positive, most power flows from the rotor terminals to the PCC, and a small portion—proportional to slip times stator power—is drawn from the BESS, causing battery discharge to stabilize the DC-link voltage. In *super-synchronous* operation, the stator delivers a small amount of power to the BESS, charging the battery to maintain DC-link voltage stability. To achieve GFM functionality, the DFIG operates on the deloaded curve with a 10% power reserve (deloading factor 0.9), as shown in Fig. 5.

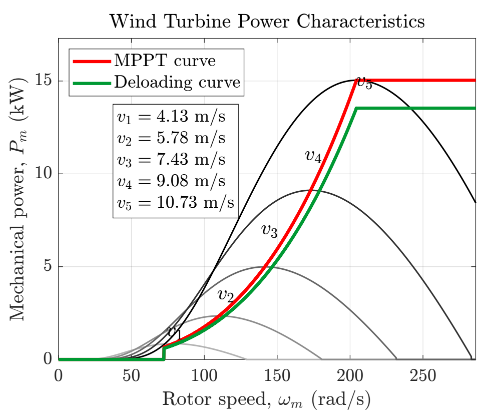

Fig. 1: Wind turbine and MPPT and Deloading curves.

B. Dynamic Modeling of DFIG

When the DFIG is controlled from the MSC on the stator side, it is generally modeled in the rotor flux reference frame [12]. The dynamic voltage equations of the DFIG in the dq reference frame can be expressed as:

$$\begin{cases} v_{ds} = R_s i_{ds} + \dfrac{d\psi_{ds}}{dt} - \omega_{sl}\psi_{qs} \\ v_{qs} = R_s i_{qs} + \dfrac{d\psi_{qs}}{dt} + \omega_{sl}\psi_{ds} \\ v_{dr} = R_r i_{dr} + \dfrac{d\psi_{dr}}{dt} - \omega_e\psi_{qr} \\ v_{qr} = R_r i_{qr} + \dfrac{d\psi_{qr}}{dt} + \omega_e\psi_{dr} \end{cases} \tag{1}$$

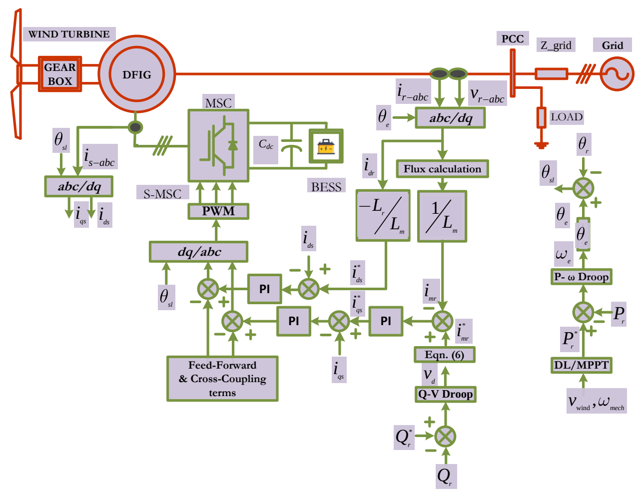

Fig. 2: Proposed control schematic diagram.

where v_{ds}, v_{qs} and v_{dr}, v_{qr} represent the stator and rotor voltages in the dq reference frame, respectively; R_s and R_r are the stator and rotor resistances; i_{ds}, i_{qs} and i_{dr}, i_{qr} denote the corresponding current components; ω_e is the synchronous electrical angular frequency; $\omega_{sl} = \omega_e - \omega_r$ is the slip angular frequency; and $\omega_r = p\omega_m$, where ω_m is the mechanical rotor speed of the DFIG.

The stator and rotor flux linkages are related to their respective current components through:

$$\begin{cases} \psi_{ds} = L_s i_{ds} + L_m i_{dr} \\ \psi_{qs} = L_s i_{qs} + L_m i_{qr} \\ \psi_{dr} = L_m i_{ds} + L_r i_{dr} \\ \psi_{qr} = L_m i_{qs} + L_r i_{qr} \end{cases} \tag{2}$$

where L_s and L_r are the stator and rotor self-inductances, and L_m denotes the mutual (magnetizing) inductance between the stator and rotor windings. The flux linking the rotor is also expressed in terms of the magnetizing current i_{mr} as:

$$\psi_r = L_m i_{mr}. \tag{3}$$

III. Proposed Control Strategy

The schematic diagram of the proposed control architecture is illustrated in Fig. 2. The control architecture is developed in the rotor reference frame with the d-axis aligned along with the rotor voltage [12], i.e., rotor-voltage orientation (RVO). Under this condition, $\psi_{dr} = 0$ and $\psi_{qr} = -\psi_r$.

Using (1)–(3) and applying RVO, the stator voltage equations can be expressed as:

$$\begin{cases} v_{ds} = R_s i_{ds} + L_s\sigma_s \dfrac{di_{ds}}{dt} - \omega_{sl}L_s\sigma_s i_{qs} + \omega_{sl}\dfrac{L_m^2}{L_r} i_{mr}, \\ v_{qs} = R_s i_{qs} + L_s\sigma_s \dfrac{di_{qs}}{dt} - \dfrac{L_m^2}{L_r}\dfrac{di_{mr}}{dt} + \omega_{sl}L_s\sigma_s i_{ds}, \end{cases} \tag{4}$$

where $\sigma_s = 1 - \dfrac{L_m^2}{L_s L_r}$ is the stator leakage coefficient.

The above set of equations forms the analytical basis for current control design in the proposed grid-forming (GFM) operation of the DFIG-based wind power system (WPS).

A. Voltage and Frequency Droop

In the proposed configuration, droop control is implemented at the rotor terminals interfaced with the PCC. The primary objective of this control scheme is to emulate the dynamic behavior of a synchronous generator by regulating the PCC voltage magnitude and frequency as functions of the measured active and reactive power exchanged with the grid.

The droop control characteristics are defined as:

$$\begin{cases} \omega_e = \omega_0 - n_P(P - P_0), \\ V_{\text{PCC}} = v_0 - n_Q(Q - Q_0), \end{cases} \tag{5}$$

where P and Q denote the instantaneous, low-pass filtered active and reactive powers at the rotor terminals, respectively; P_0 and Q_0 are the reference active and reactive power setpoints; and n_P and n_Q represent the active and reactive power droop coefficients.

The droop-generated reference quantities (v^*, ω_e^*) are subsequently supplied to the inner control loops of the MSC to regulate voltage and frequency under grid-forming operation.

B. Magnetizing Current Control

The magnetizing current control loop regulates the air gap flux, which indirectly determines the rotor voltage of the machine. In the proposed hierarchical structure, the reference value of the magnetizing current is generated from the outer droop-based voltage–frequency references (v^*, ω_e^*). Using the steady-state flux–voltage relation under RVO, i_{mr}^* is computed as:

$$i_{mr}^* = \frac{v_{dr}^*}{\omega_e^* L_m}, \tag{6}$$

The dynamic relation between the controllable q-axis rotor current i_{qr} and the magnetizing current i_{mr} is described by the q-axis rotor equation under RVO as:

$$v_{qr} = R_r i_{qr} + \frac{d\psi_{qr}}{dt}, \tag{7}$$

Further using (7) and substituting $\psi_{qr} = -L_m i_{mr}$ yields the dynamic relationship between i_{mr} and i_{qs} as:

$$\tau_{mr}\frac{di_{mr}}{dt} + i_{mr} = i_{qs} + \frac{L_r}{L_m R_r} v_{qr}, \tag{8}$$

where $\tau_{mr} = \frac{L_r}{R_r}$ is the rotor time constant.

The term $\frac{L_r}{L_m R_r} v_{qr}$ acts as a constant feed-forward term. Thus, the transfer function from i_{qs} to i_{mr} can be written as:

$$\frac{I_{mr}(s)}{I_{qs}(s)} = \frac{1}{\tau_{mr}s + 1}, \tag{9}$$

A proportional–integral (PI) controller ensures accurate tracking of the reference i_{mr}^*. The actual i_{mr} is obtained via flux calculation. The control law is expressed as:

$$i_{qs}^* = K_{pm}\big(i_{mr}^* - i_{mr}\big) + K_{im}\int\big(i_{mr}^* - i_{mr}\big)dt + \frac{L_r}{L_m R_r} v_{qr}, \tag{10}$$

The PI controller gains are obtained by matching the closed-loop characteristic polynomial to a standard second-order prototype, which yields:

$$K_{pm} = 2\zeta_m \omega_{nm}\tau_{mr} - 1, \qquad K_{im} = \omega_{nm}^2 \tau_{mr}, \tag{11}$$

With proper choice of ζ_m and ω_{nm}, K_{pm} and K_{im} are computed. The output of this control loop is i_{qs}^*. Furthermore, the d-axis stator current holds a control freedom and the desired value is obtained simply as:

$$i_{ds}^* = -\frac{L_r}{L_m} i_{dr} \tag{12}$$

C. Current Control Loops

The innermost control layer of the proposed system is implemented on the machine-side converter (MSC), which directly regulates the stator currents (i_{ds}, i_{qs}). The PI-based control laws for this stage are expressed as:

$$\begin{cases} v_{ds}^* = K_{pd}e_{ids} + K_{id}\int e_{ids}\,dt - \omega_{sl}L_s\sigma_s i_{qs} + \omega_{sl}\dfrac{L_m^2}{L_r} i_{mr}, \\ v_{qs}^* = K_{pq}e_{iqs} + K_{iq}\int e_{iqs}\,dt + \omega_{sl}L_s\sigma_s i_{ds} - \dfrac{L_m^2}{L_r}\dfrac{di_{mr}}{dt}, \end{cases} \tag{13}$$

where $e_{ids} = (i_{ds}^* - i_{ds})$ and $e_{iqs} = (i_{qs}^* - i_{qs})$. The inner loops are generally designed with faster response, which ensures that the rotor magnetizing current is accurately tracked, and hence the desired voltage and frequency at the rotor terminals. The reference voltages (v_{ds}^*, v_{qs}^*) are transformed into three-phase variables, yielding the modulation commands $(v_{s,abc}^*)$ for the PWM block. These determine the gating signals (S_{abc}) applied to the MSC.

IV. Simulation Results and Discussion

This section presents MATLAB/Simulink results validating the proposed rotor-side grid-forming (GFM) control strategy under varying wind, load, and grid conditions. Three composite figures are used to illustrate the dynamic behavior of the system. Figure 4 shows the wind and mechanical speed along with the evolution of active and reactive power governed by the droop-stage references. Figure 5 illustrates the magnetizing current control (MCC), the stator/rotor current responses, and the dc-link regulation. Figure 6 presents the overall power balancing among the stator, rotor, grid, load, and battery. The parameters of the wind turbine and DFIG system are listed in Table I.

A. Dynamic Behavior Under Droop-Based GFM Operation

At $t = 0$ s, the grid is connected, the load is 7 kW, and the wind speed is 9.08 m/s. As shown in Fig. 4(a), the wind-speed input initiates deloaded operation, and the droop-generated reference rotor power (P_r) accelerates the rotor to its

979-8-3315-8138-1

steady-state mechanical speed ω_m, depicted in Fig. 4(b). The measured rotor power tracks its reference through the $(P-\omega)$ droop controller, while the $(Q-V)$ droop loop produces the PCC voltage reference v, which aligns with the d-axis voltage (v_{ds}). This behavior is visible in the subplots of P_r, Q_r, and their respective droop-generated outputs in Fig. 4(c)–(f).

Because the system operates under weak-grid conditions, the stator flux cannot self-stabilize. Consequently, MCC is activated to regulate the rotor magnetizing current such that $i_{mr} \rightarrow i_{mr}$ as dictated by (6), thereby stabilizing the rotor flux vector and enabling indirect rotor flux orientation (IDRFO). The corresponding trajectories of ψ, ψ_{dr}, ψ_{qr}, and the reference–actual magnetizing currents are shown in Fig. 5(a)–(b). MCC generates the reference i_{qs}, while i^*_{ds} is obtained from (12). These stator current references are accurately tracked by the inner PI current loops, as seen in Fig. 5(c)–(d). The coordination among the droop controller, MCC, and the inner current loops ensures that the MSC synthesizes the desired rotor-terminal voltage and frequency under all operating events.

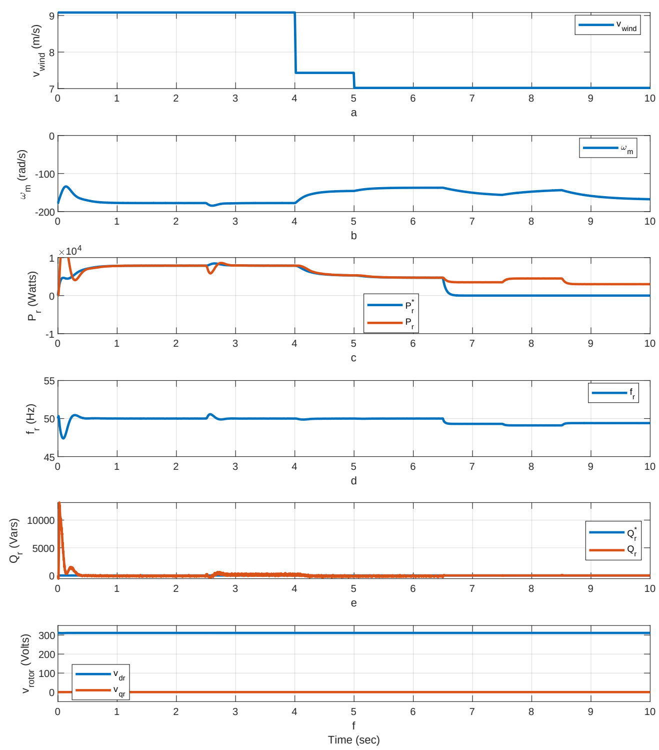

Fig. 3: Dynamic response of the droop stage variables.

B. *Response to Sequential Operating Events*

The system undergoes several sequential events, and its responses can be observed collectively in Figs. 4–6. Initially, at $t = 0$ s, the GFM functionality establishes the rotor-terminal voltage and frequency while the rotor supplies the load and injects the surplus power into the grid. The dc-link remains regulated as the BESS dynamically exchanges power with the stator (Fig. 6(a)–(b)).

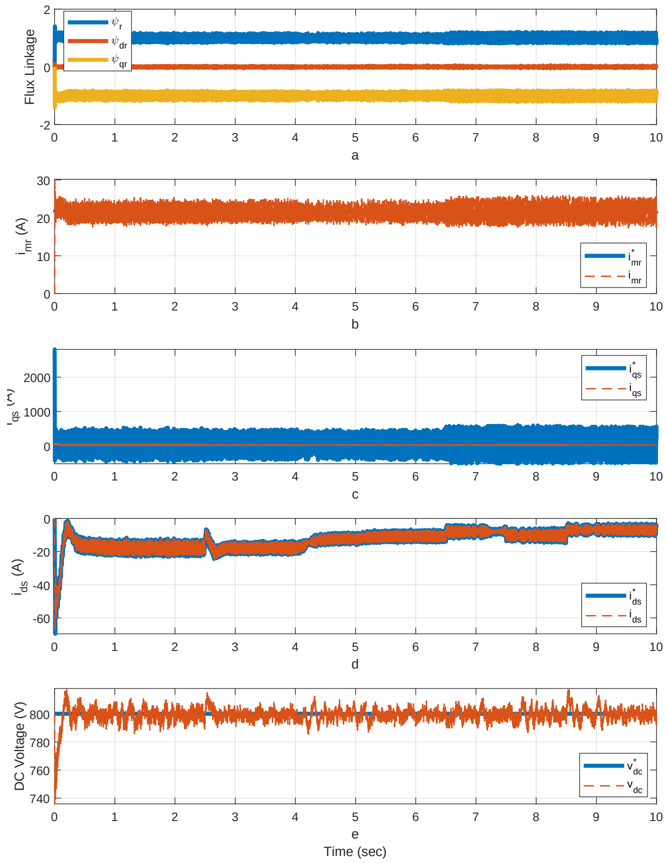

Fig. 4: Power flow variations among system components.

At $t = 2.5$ s, the load decreases from 7 kW to 3.5 kW. Since the rotor power remains unchanged, the reduction in load results in an increase in power injected into the grid, as seen in Fig. 6. Correspondingly, the battery absorbs surplus power generated through the stator due to the supersynchronous operation of the rotor (Fig. 4(b)), while maintaining a stiff dc link.

At $t = 4$ s, the wind speed falls from 9.08 m/s to 7.4 m/s, shifting the rotor into subsynchronous operation, as presented in Fig. 4(b). Rotor power output decreases accordingly, causing the stator to absorb power from the battery (Fig. 6(a)–(b)). The BESS compensates by discharging power to maintain dc-link stability.

A further wind-speed reduction at $t = 5$ s (from 7.4 m/s to 7.02 m/s) increases the discharge demand on the battery, as shown in Fig. 6(b). Throughout this period, rotor flux and currents remain stable (Fig. 5), demonstrating the robustness of MCC under varying wind conditions.

At $t = 6.5$ s, an unexpected grid disconnection occurs. The rotor-side GFM controller quickly transitions the system into standalone operation. Grid power immediately drops to zero (Fig. 6(a)–(b)), and the DFIG–BESS combination solely supplies the load. Voltage and frequency remain stable during the transition, as evidenced in Fig. 4(d)–(f), confirming the autonomous GFM capability.

979-8-3315-8138-1

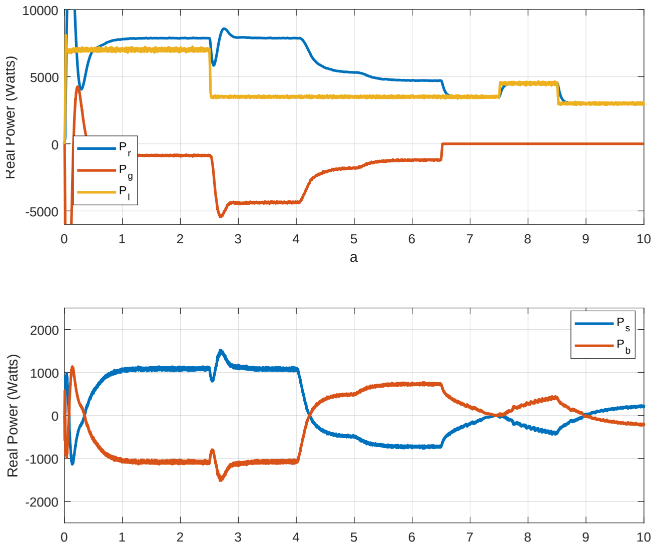

Fig. 5: Dynamic response of inner current loop and DC-bus variables.

Finally, at $t = 7.5$ s, the load increases from 3.5 kW to 4.5 kW in islanded mode. The droop controller adjusts the rotor power accordingly, and rotor voltage regulation is sustained (Fig. 4(f)), with a small frequency deviation observed in Fig. 4(d). At $t = 8.5$ s, the load decreases again to 3 kW, and both stator and rotor powers settle at lower levels (Fig. 6(a)–(e)). The battery absorbs the excess power, and the dc-link voltage remains tightly regulated throughout the event.

Across all operating events—including wind-speed variations, load changes, and the grid trip—the proposed rotor-side GFM strategy consistently maintains stable voltage and frequency at the rotor terminals, demonstrating reliable grid-forming capability in both grid-connected and standalone modes. The MCC effectively stabilizes the flux and magnetizing currents under weak-grid conditions and during islanding, while the inner current controllers ensure smooth and accurate stator and rotor current tracking. Throughout all transitions, the dc-link voltage remains tightly regulated by the BESS, which seamlessly compensates for power deficits and absorbs surplus energy. Overall, the coordinated operation of the droop controller, MCC, and current loops enables robust and stable dynamic performance across all scenarios.

V. Conclusion

This paper presented a rotor-side grid-forming (GFM) control strategy for a Type-III DFIG, marking the first work to demonstrate full GFM functionalities directly at the rotor terminals of a Type-III wind turbine. A detailed dynamic model under rotor-voltage orientation was developed, and a hierarchical control architecture—comprising droop control, magnetizing current control, and inner current loops—was proposed. The configuration eliminates the need for a dedicated grid-side converter while enabling bidirectional energy exchange through the dc link. Simulation results verified stable PCC voltage and frequency, effective dc-link regulation, and seamless power balancing during wind-speed variations, load changes, and grid disconnection. The framework provides a compact and efficient solution for wind power systems requiring grid-forming capability and enhanced operational flexibility. Future research will focus on integrating adaptive droop mechanisms and virtual synchronous generator (VSG) functionalities, advancing black-start capability, enabling smooth transitions between grid-connected and islanded modes, and improving resilience during extreme disturbances.

TABLE I: Wind Turbine and DFIG Parameters

Parameter	**Value**
Rated Power	15 kW
Rated Voltage	$220\sqrt{3}$ V
Number of Pole Pairs	2
Stator Resistance R_s	161 mΩ
Stator Inductance L_s	3 mH
Rotor Inductance L_r	3 mH
Mutual Inductance L_m	46.5 mH
Rotor Resistance R_r	178 mΩ
Inertia J	$0.2\,\mathrm{kg}\cdot\mathrm{m}^2$
Friction Coefficient B	1×10^{-3}
Gearbox Ratio N	10
Turbine Radius	3.7848 m

References

[1] Global Wind Energy Council, *Global Wind Report 2025*. Lisbon, Portugal: GWEC, Apr. 2025.

[2] X. Wang, M. G. Taul, H. Wu, Y. Liao, F. Blaabjerg, and L. Harnefors, “Grid-synchronization stability of converter-based resources—An overview,” *IEEE Open J. Ind. Appl.*, vol. 1, pp. 115–134, 2020.

[3] R. H. Lasseter, Z. Chen, and D. Pattabiraman, “Grid-forming inverters: A critical asset for the power grid,” *IEEE J. Emerg. Sel. Top. Power Electron.*, vol. 8, no. 2, pp. 925–935, 2020.

[4] Y. Li, Y. Gu, and T. Green, “Revisiting grid-forming and grid-following inverters: A duality theory,” *IEEE Trans. Power Syst.*, vol. 37, pp. 4541–4554, 2022.

[5] J. Fang, H. Li, Y. Tang, and F. Blaabjerg, “On the inertia of future more-electronics power systems,” *IEEE J. Emerg. Sel. Topics Power Electron.*, vol. 7, no. 4, pp. 2130–2146, 2019, doi: 10.1109/JESTPE.2018.2877766.

[6] L. Huang, H. Xin, L. Zhang, Z. Wang, K. Wu, and H. Wang, ”Synchronization and frequency regulation of DFIG-based wind turbine generators with synchronized control,” *IEEE Trans. Energy Convers.*, vol. 32, no. 3, pp. 1251-1262, Sep. 2017, doi: 10.1109/TEC.2017.2675480.

[7] R. K. Rastogi and R. Sharma, ”Improved synchronization and voltage regulation of DFIG based wind energy system (WES),” in *Proc. Int. Conf. Curr. Trends Towards Converging Technol.*, 2018. pp. 1-5, doi: 10.1109/ICCTCT.2018.8551121.

[8] Y. Han and J.-I. Ha, ”Droop control using impedance of grid-integrated DFIG within microgrid,” *IEEE Trans. Energy Convers.*, vol. 34, no. 1, pp. 88-97, Mar. 2019, doi: 10.1109/TEC.2018.2861819.

[9] H. Xiao, Z. Zhao, K. Zhou, J. Guo, C. S. Lai, and L. Lei Lai, ”Voltage source control of DFIG in standalone wind power-based microgrids,” in *Proc. IEEE 1st China Int. Youth Conf. Elect. Eng.*, 2020, pp. 1-7, doi: 10.1109/CIYCEE49808,2020,9332674.

[10] N. David and D. C. Aliprantis, ”Improved efficiency of DFIG wind energy conversion systems by operating in the rotor-tied configuration,” in *Proc. 2014 Int. Conf. Elect. Mach. (ICEM)*, Sep. 2014, pp. 189–195.

[11] Y. M. You, T. A. Lipo, and B. Il Kwon, ”Design and analysis of a novel grid-connected to rotor type doubly fed induction machine,” *IEEE Trans. Magn.*, vol. 48, no. 2, pp. 919–922, 2012.

[12] R. M. Prasad and M. A. Mulla, ”Mathematical Modeling and Position-Sensorless Algorithm for Stator-Side Field-Oriented Control of Rotor-Tied DFIG in Rotor Flux Reference Frame,” *IEEE Trans. Energy Convers.*, vol. 35, no. 2, pp. 631-639, Jun. 2020, doi: 10.1109/TEC.2019.2956255.

979-8-3315-8138-1